JACS
JOURNAL OF THE AMERICAN CHEMICAL SOCIETY
Article
Cite This: J. Am. Chem. Soc. 2019, 141, 18142−18151
pubs.acs.org/JACS

Structure, Dynamics, and Reactivity for Light Alkane Oxidation of Fe(II) Sites Situated in the Nodes of a Metal−Organic Framework

Matthew C. Simons,[†] Jenny G. Vitillo,[‡] Melike Babucci,[§] Adam S. Hoffman,[∥] Alexey Boubnov,[∥] Michelle L. Beauvais,[⊥] Zhihengyu Chen,[⊥] Christopher J. Cramer,[‡] Karena W. Chapman,[⊥] Simon R. Bare,[∥] Bruce C. Gates,[§] Connie C. Lu,[‡] Laura Gagliardi,*[,‡] and Aditya Bhan*[,†]

[†]Department of Chemical Engineering and Materials Science, University of Minnesota, 421 Washington Avenue SE, Minneapolis, Minnesota 55455, United States
[‡]Department of Chemistry, Chemical Theory Center, and Supercomputing Institute, University of Minnesota, 207 Pleasant Street SE, Minneapolis, Minnesota 55455, United States
[§]Department of Chemical Engineering, University of California, Davis, California 95616, United States
[∥]SSRL, SLAC National Accelerator Laboratory, Menlo Park, California 94025, United States
[⊥]Department of Chemistry, Stony Brook University, 100 Nicolls Road, Stony Brook, New York 11794, United States

Supporting Information

ABSTRACT: Metal organic frameworks (MOFs), with their crystalline, porous structures, can be synthesized to incorporate a wide range of catalytically active metals in tailored surroundings. These materials have potential as catalysts for conversion of light alkanes, feedstocks available in large quantities from shale gas that are changing the economics of manufacturing commodity chemicals. Mononuclear high-spin ($S = 2$) Fe(II) sites situated in the nodes of the MOF MIL-100(Fe) convert propane via dehydrogenation, hydroxylation, and overoxidation pathways in reactions with the atomic oxidant N_2O. Pair distribution function analysis, N_2 adsorption isotherms, X-ray diffraction patterns, and infrared and Raman spectra confirm the single-phase crystallinity and stability of MIL-100(Fe) under reaction conditions (523 K in vacuo, 378−408 K C_3H_8 + N_2O). Density functional theory (DFT) calculations illustrate a reaction mechanism for the formation of 2-propanol, propylene, and 1-propanol involving the oxidation of Fe(II) to Fe(III) via a high-spin Fe(IV)=O intermediate. The speciation of Fe(II) and Fe(III) in the nodes and their dynamic interchange was characterized by in situ X-ray absorption spectroscopy and ex situ Mössbauer spectroscopy. The catalytic relevance of Fe(II) sites and the number of such sites were determined using in situ chemical titrations with NO. N_2 and C_3H_6 production rates were found to be first-order in N_2O partial pressure and zero-order in C_3H_8 partial pressure, consistent with DFT calculations that predict the reaction of Fe(II) with N_2O to be rate determining. DFT calculations using a broken symmetry method show that Fe-trimer nodes affecting reaction contain antiferromagnetically coupled iron species, and highlight the importance of stabilizing high-spin ($S = 2$) Fe(II) species for effecting alkane oxidation at low temperatures (<408 K).

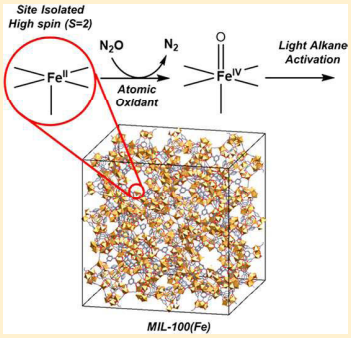

INTRODUCTION

The abundance of light alkanes in natural gas and shale gas has invigorated efforts aimed at maximizing the value of these compounds as chemical feedstocks. Activation of light alkanes without combustion is challenging; their oxidative functionalization requires the intervention of reactive species capable of breaking apolar C−H bonds while limiting overoxidation of products that contain progressively weaker C−H bonds.[1] Enzymes overcome these challenges using metal-oxo species that require energy inputs from coupled reactions and a series of gating mechanisms aided by complex channel environments to control access to the active site to prevent overoxidation.[2,3] One strategy in the design of tailored catalysts for selective light alkane activation is to mimic the functions and characteristics of enzymes within solid supports.[4]

Steps toward designing such tailored catalysts have focused on understanding the reactivity of nonheme iron sites in enzymes that activate alkanes, notably the high-spin, di-iron sites in methane monooxygenase[3,5] and monoiron sites in enzymes such as TauD.[6] Isolating similar iron species on solid supports thus constitutes a major area of focus today.[7−12] Metal organic frameworks (MOFs)—modular, crystalline materials constituted of organic linkers and inorganic nodes—are ideal target supports for iron sites for light alkane activation. The multitude of compositions and topologies in porous structures that MOFs afford[13−16] commend them for design of materials with structural features that mimic functional characteristics of enzymes. Thus MOFs are ideal

Received: August 11, 2019
Published: October 31, 2019

DOI: 10.1021/jacs.9b08686
J. Am. Chem. Soc. 2019, 141, 18142−18151

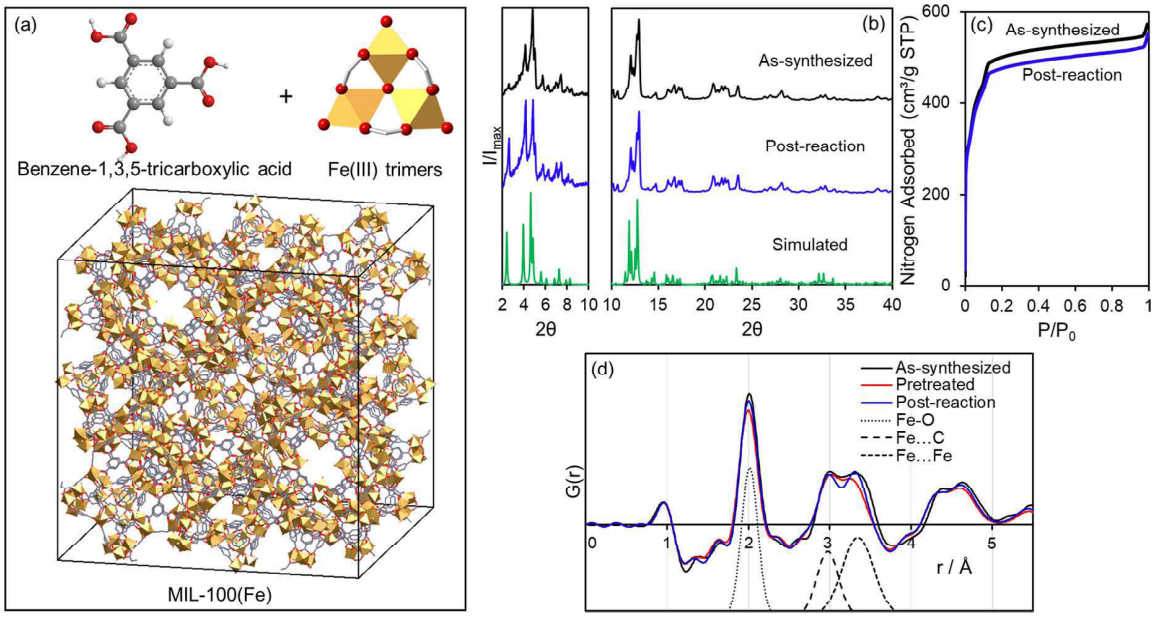

Figure 1. (a) Schematic representation of the unit cell of MIL-100(Fe) ($Fd\bar{3}m$, a = 70.74 Å) with its constituent node and linker (Fe, orange octahedra; O, red; C, gray; H, white). (b) XRD pattern of MIL-100(Fe) as-synthesized and postreaction compared with the simulated pattern for MIL-100. (c) N_2 adsorption isotherm at 77 K for MIL-100(Fe) as-synthesized (Langmuir surface area = 2236 m^2 g^{-1}) vs postreaction (2150 m^2g^{-1}). (d) Ex situ differential PDF of MIL-100(Fe) as-synthesized, after pretreatment in vacuo at 523 K, after reaction with N_2O/C_3H_8 at 398 K, determined by subtracting the PDF of the organic linker (benzene-1,3,5-tricarboxylic acid) from the PDF of MIL-100(Fe).

supports for iron sites for light alkane oxidation. MOFs proposed to contain biomimetic mono- and dinuclear iron sites capable of activating light alkanes include MOF-74-(Mg, Fe)[17,18] and MIL-53(Fe, Al),[19] respectively, and computational evidence suggests an expanded library of MOFs may contain sites capable of effecting light alkane activation.[20−22]

The ability of MIL-100(Fe)[23] to form unsaturated Fe(II) species upon thermal treatment has been reported on the basis of infrared (IR) and Mössbauer spectroscopy.[24−26] These Fe species are similar in geometry and oxidation state to those proposed for Fe-exchanged zeolites (BEA,[10,11] CHA[12]) and MOF-74-(Mg, Fe),[19,20] leading us to postulate that these sites in MIL-100(Fe) might be capable of activating light alkanes.

Herein, we report that such activation occurs using MIL-100(Fe), having characterized its reactions with propane and ethane and its function as a catalyst for converting propane to hydroxylation, dehydrogenation, and over-oxidation products with N_2O as the oxidant. Because work with these and related MOFs has not yet included reaction kinetics or detailed characterization of the active site,[27] and because such information is required for understanding the reactivity at the level of elementary reaction steps, we used a set of complementary methods to gain such understanding. Thus, we demonstrate that trimeric Fe-oxo containing nodes, common building units in a wide library of existing MOFs including MIL-100(Fe),[28] contain sites capable of activating light alkanes, opening a new and promising platform upon which to design new catalytic materials.

MIL-100(Fe) was synthesized by reported protocols,[29] and the crystallinity, phase purity, and integrity of the framework before and after reaction were determined with N_2 adsorption, pair distribution function (PDF) analysis, powder X-ray diffraction, and IR and Raman spectroscopies. Catalyst performance was investigated with mixtures of C_3H_8 + N_2O fed to a recirculating batch reactor working at temperatures between 378 and 408 K after catalyst pretreatment at 523 K in vacuo—resulting in formation of propylene in the gas phase and C_3-oxygenates adsorbed within the MOF, which were released by washing in D_2O ex situ. In situ probe molecule titrations in concert with Kohn−Sham density functional theory (DFT), X-ray absorption spectroscopy (XAS), Mössbauer spectroscopy, and IR spectroscopy were used to ascertain the identity, relevance, and number of coordinatively unsaturated, mononuclear, high-spin (S = 2), Fe(II) active sites situated in the nodes of MIL-100(Fe), sites that mimic the nuclearity, spin state, and oxidation of iron sites in enzymes such as TauD. A combination of reaction kinetics and DFT calculations shows that the rate limiting reaction involves the Fe(II) site reacting with N_2O to form a high-spin Fe(IV)═O moiety, which proceeds to activate propane through hydrogen atom abstraction (HAA) and subsequent conversion to propanol via a rebound mechanism, or a further HAA for conversion to propylene.

EXPERIMENTAL AND COMPUTATIONAL METHODS

Synthesis of MIL-100(Fe). MIL-100(Fe) was synthesized according to a reported procedure.[29] Details of the synthesis procedure and details of N_2 adsorption isotherms, powder X-ray diffraction patterns, and Raman and IR spectroscopy are included in Section S1 of the SI.

Catalytic Reaction Experiments. Catalytic tests were performed with two recirculating batch reactor systems, described in detail in Section S1 in the SI.

Pair Distribution Function (PDF) Analysis. Details on sample preparation are given in Section S1 of the SI. Data for pair distribution function analysis were collected at beamline 11-ID-B of the Advanced Photon Source at Argonne National Laboratory using an X-ray wavelength of 0.2114 Å. The PDFs, $G(r)$, were extracted within xPDFsuite[30] following calibration and integration of the diffraction images in GSAS-II.[31]

DOI: 10.1021/jacs.9b08686
J. Am. Chem. Soc. 2019, 141, 18142−18151

Table 1. EXAFS Fit Parameters Characterizing MIL-100(Fe) under Various Conditions

sample	shell	N^a	R (Å)	$\Delta\sigma^2$ (Å^2)	ΔE_0 (eV)
MIL-100(Fe)[b] as-synthesized	Fe−O_1	5.0 ± 0.4	1.96 ± 0.06	0.006 ± 0.003	6.56 ± 1.70
	Fe−O_2	1.0 ± 0.4	2.05 ± 0.04	0.005 ± 0.002	
	Fe−C	4.0 ± 0.2	2.97 ± 0.18	0.005 ± 0.003	
	Fe−O_3	4.0 ± 0.3	3.16 ± 0.05	0.010 ± 0.006	
	Fe−Fe	2.0 ± 0.1	3.41 ± 0.01	0.014 ± 0.006	
MIL-100(Fe) pretreated	Fe−O_1	4.7 ± 0.4	1.99 ± 0.09	0.006 ± 0.003	6.56 ± 1.70
	Fe−O_2	0.3 ± 0.1	2.06 ± 0.05	0.005 ± 0.002	
	Fe−C	4.0[c]	2.95 ± 0.16	0.005 ± 0.003	
	Fe−O_3	4.0[c]	3.16 ± 0.05	0.010 ± 0.006	
	Fe−Fe	2.0[c]	3.40 ± 0.02	0.014 ± 0.006	
MIL-100(Fe) post-reaction (after N_2O + C_2H_6 flow)	Fe−O_1	5.2 ± 0.6	1.98 ± 0.08	0.004 ± 0.002	6.56 ± 1.70
	Fe−O_2	1.1 ± 0.3	2.07 ± 0.06	0.005 ± 0.002	
	Fe−C	4.0[c]	2.98 ± 0.17	0.005 ± 0.003	
	Fe−O_3	4.0[c]	3.18 ± 0.03	0.008 ± 0.002	
	Fe−Fe	2.0[c]	3.42 ± 0.01	0.009 ± 0.003	

[a]Notation: N, coordination number; R, distance between the absorber and backscattering atoms; $\Delta\sigma^2$, mean square relative displacement; ΔE_0, inner potential correction. O_1 denotes single scattering Fe−O_1, O_2 denotes single scattering Fe−O_2, and O_3 denotes single scattering Fe−O_3 (see Figure S14 in the SI for details). [b]For comparison, coordination numbers and distances characterizing as-synthesized MIL-100(Fe) optimized by DFT calculations are the following: Fe−O_1 (N: 5.0, R: 1.90 Å), Fe−O_2 (N: 1.0, R: 2.01 Å), Fe−C (N: 4.0, R: 2.79 Å), Fe−O_3 (N: 4.0, R: 3.21 Å), Fe−Fe (N: 2.0, R: 3.42 Å). [c]These values were fixed in the modeling. S_0^2 of MIL-100(Fe) is 0.84 ± 0.04 refined from α-Fe_2O_3 (Figures S15−16). Figure S14 illustrates the scattering paths used in the EXAFS analysis. The range in k was 3.5−12.9 Å^{-1}, and the range in r was 1.0−4.0 Å.

X-ray Absorption Spectroscopy. XAS measurements were made at beamline 9−3 at the Stanford Synchrotron Radiation Lightsource (SSRL). Continuous extended X-ray absorption fine structure (EXAFS) spectra were measured at 308 K from 200 eV below the Fe K-edge (7112 eV) to k = 15.3 Å^{-1} (k is the wavenumber) in a period of 4 min, with three scans collected and averaged to improve the signal-to-noise ratio under all conditions. Further details, including the analysis of the EXAFS data, are provided in Sections S1 and S6 in the SI.

Mössbauer Spectroscopy. ^{57}Fe Mössbauer spectra were recorded at liquid helium temperatures (18 K). One sample was prepared after pretreatment in vacuo at 523 K for 10 h, with the sample sealed with Swagelok quick-connect fittings and transferred to a N_2-filled glovebox to prevent air exposure, loaded into a sample holder sealed with parafilm, and transferred to the spectrometer. Further details are listed in Sections S1 and S7 of the SI.

Kohn−Sham Density Functional Theory Calculations. DFT calculations were performed using the M06-L functional[32] in its unrestricted formalism (U) in combination with the def2-TZVP basis sets,[33,34] as implemented in the *Gaussian 16* program.[35] Previous investigations showed that this level of theory correctly reproduces electronic properties of iron centers in MOFs,[18] in particular the tri-iron-oxo-centered cluster when benchmarked to multireference calculations.[36] Further details are presented in Sections S1 and S9 in the SI.

RESULTS AND DISCUSSION

Synthesis, Structure, and Reaction Scheme. MIL-100(Fe)[23] is a MOF comprising trimeric Fe(III)-oxo nodes and benzene-1,3,5-tricarboxylic acid-derived linkers that form a crystalline framework with 25 and 29 Å diameter cages accessible through 5.5- and 8.6-Å diameter windows (Figure 1a). MIL-100(Fe) was synthesized in gram quantities according to a reported HF-free procedure.[29] XRD patterns (Figure 1b) of the as-synthesized material show the exclusive presence of the MIL-100 phase. The Langmuir surface area of 2236 m^2 g^{-1} (Figure 1c) and Raman (Figure S1 in the SI) and IR (Figure S2) spectra closely resemble those reported for MIL-100(Fe).[25,37,38] Hydroxy groups, often associated with local defects and structural collapse in MOFs, were found to be present in the as-synthesized MOF but after treatment in vacuo at 473 K, no signals associated with hydroxy groups could be detected in the 3700−3300 cm^{-1} range of the IR spectrum (light gray line in Figure S2). These bands are likely associated with solvent molecules in the MOF pores and hydroxy groups on the nodes. Modeling of EXAFS spectra (Table 1), discussed in detail below, also show excellent agreement with a single-node model of MIL-100(Fe) optimized by DFT (Section S9.3 in the SI), providing further evidence that MIL-100(Fe) as synthesized incorporates well-defined Fe(III) trimer nodes and organic linkers.

Unsaturated Fe(II) species have been proposed to serve as the active sites in zeolites[10−12] and MOFs[17,18] capable of activating light alkanes through an Fe(IV)=O intermediate formed with the oxygen-atom transfer reagent, N_2O. Mössbauer and IR spectra have shown that trivalent Fe atoms located in the nodes of MIL-100(Fe), as synthesized, undergo dynamic changes in both coordination and oxidation state when subjected to high-temperature (<533 K) treatment in vacuo,[24−26] notably resulting in the creation of unsaturated Fe(II) sites. One of our goals was to explore the identity and reactivity of such sites and to quantify these, or other, sites that can activate light alkanes with an oxo-transfer agent.

An initial stepped reaction scheme was proposed to test the reactivity of MIL-100(Fe) for light alkane activation through successive exposures of the catalyst to N_2O and C_3H_8.[7,8,38] Quantitative yields of N_2 were detected during exposure of MIL-100(Fe) to N_2O (Figure S3); however, no carbon-containing products were observed in the gas phase (Figure S4) or in the products of subsequent solvent washes carried out ex situ. In contrast, when N_2O and C_3H_8 were fed together, yields of N_2 were observed—at initial rates identical to those resulting upon exposure to N_2O alone (Figure S5)—along with propylene in the gas phase. 2-Propanol, 1-propanol, acetone, and 1,2- and 1,3- propane diol were observed using ^{1}H NMR spectroscopy as major products released after washing the catalyst with D_2O ex situ (Figure 2).

A similar scheme was reported for the conversion of ethane to ethanol with MOF-74-(Mg,Fe), and the results were

DOI: 10.1021/jacs.9b08686
J. Am. Chem. Soc. 2019, 141, 18142−18151

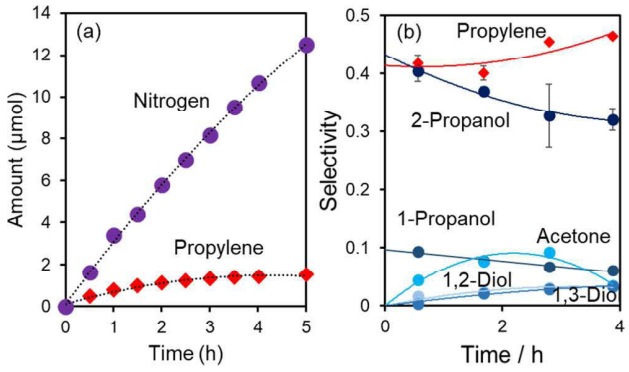

Figure 2. (a) Yield of gas-phase products in a batch reactor for an illustrative N_2O + C_3H_8 experiment (45 mg MIL-100(Fe), 393 K, $P_{total,t=0}$ = 114 kPa, $P_{N_2O,t=0}$ = 35 kPa, $P_{C_3H_8,t=0}$ = 1.3 kPa). (b) Selectivity vs batch time for gas-phase and adsorbed products after ex situ quantification (40 mg MIL-100(Fe), 393 K, $P_{total,t=0}$ = 114 kPa, $P_{N_2O,t=0}$ = 35 kPa, $P_{C_3H_8,t=0}$ = 2.4 kPa). Adsorbed products: 2-propanol, 1-propanol, acetone, propane-1,2-diol (1,2-Diol), and propane-1,3-diol (1,3-Diol).

inferred to be indicative of an unstable Fe(IV)=O moiety as an intermediate species.[17] Similarly we found that MIL-100(Fe) is able to activate the sp^3 C–H bond in C_2H_6 (Figures S6 and S7), but we proceeded with an investigation of C_3H_8 rather than C_2H_6 because of our ready ability to quantify products and to close carbon balances around C_3H_8 consumption. However, C_2H_6 was used instead of C_3H_8 in our in situ XAS experiments as its simpler chemistry allowed us to focus on the iron speciation and oxidation state.

In the reaction experiments, we sought information on the product rank to give further insight into the reaction pathways. Thus, we observed changes in product selectivity as a function of time in the batch reactor; products with nonzero selectivity when extrapolated to t = 0 were formed directly from propane, and products with zero selectivity at t = 0 formed in subsequent reaction steps. This analysis required independent experiments at identical temperature and initial reactant partial pressures with the reaction stopped at different times in order to develop a profile of selectivity vs time (Figure 2b) because of the need to wash the catalyst ex situ to quantify strongly adsorbed oxygenate products. Propylene, 2-propanol, and 1-propanol were found to have nonzero selectivity at zero conversion/time, demonstrating that these three products form directly from propane. All other oxygenate products were found to have zero selectivity at t = 0, implying they are secondary (or higher) ranked products. These results provide evidence that MIL-100(Fe) functions by oxidizing substrates sequentially; i.e., the active site oxidizes a substrate once before enabling the product to desorb.

Propylene formed in high yields relative to the two alcohol products (Figure 2). This is atypical, as the common mechanism invoked to explain the reactivity of Fe-oxo species for alkane activation is radical rebound to form hydroxylated products. While oxidative dehydrogenation in MOFs has been studied previously,[39,40] the different metal (Co) and oxidant (O_2) lead us to discount the proposed Mars van Krevelen-type mechanism for dehydrogenation for our system, and instead propose an alternate mechanism—corroborated by DFT calculations—involving secondary C–H abstraction instead of radical rebound to form propylene (vide infra). Also contrasted with our results are those reported for Fe-MOF-74, which gave no dehydrogenated products from ethane.[17]

N_2 isotherms and XRD patterns demonstrate that the surface area, phase purity, and crystallinity of MIL-100(Fe) were retained after reaction and washing of the used catalyst (Figure 1b,c). Thus, we conclude that MIL-100(Fe) catalyzed light alkane oxidation with N_2O while retaining its bulk characteristics.

We sought further insight into the structural changes of the MIL-100(Fe) nodes after pretreatment and reaction using ex situ PDF analysis. The PDFs of MIL-100(Fe) as-synthesized, after pretreatment in a vacuum at 523 K, and after exposure to N_2O + C_3H_8 at 393 K (Figure S8) show that local and long-range MIL-100(Fe) structure[41] was maintained throughout, without the appearance of secondary species that might catalyze alkane activation, such as nanoparticles of iron that have been observed in zeolites by transmission electron microscopy.[42] Changes in bonding within MIL-100(Fe) were observed as a result of treating the as-synthesized material in vacuo at 523 K; these changes were reversed to a degree after the catalytic reaction at 393 K. Differential PDFs, which isolate the iron-containing node coordination geometry by subtracting the PDF of the benzene-1,3,5-tricarboxylic acid-derived linkers from that of the MOF (Figure 1d), show that average Fe–O bonds decreased from 2.015 to 2.001 Å in length and that the average Fe–Fe distance within the node decreased from 3.347 to 3.310 Å during pretreatment at 523 K in vacuo. The relative intensity of the Fe–O peak decreased as a result of activation, consistent with a reduction in the average iron coordination number. The intensity (and thus coordination) was partially recovered (Table S1) during reaction with N_2O + C_3H_8, and the interatomic distances partially recovered to 2.009 and 3.343 Å for Fe–O and Fe–Fe, respectively. The average Fe–C distance (2.993 Å) decreased to 2.973 Å after pretreatment and recovered to 2.980 Å after reaction. These changes in bond length and coordination environment within the nodes are consistent with EXAFS results discussed below.

Identity and Number of Active Sites. Site-specific characterization techniques were used to identify the nature of the active Fe sites and explore changes during reaction (Section S6 in the SI). In situ Fe K-edge XAS data were collected to probe the local structure of Fe within MIL-100(Fe) at three different stages of the reaction scheme: as-synthesized, after pretreatment in flowing helium at 523 K, and after reaction in the presence of N_2O + C_2H_6 at 393 K (Figure 3).

A comparison of the X-ray absorption near edge structure (XANES) data of the three states of the catalyst (Figure 3a) shows that, as a result of the pretreatment, there was a shift of the absorption edge to lower energy, accompanied by changes in the pre-edge peaks (inset of Figure 3a). There was also a decrease in the magnitude of the Fourier transform (FT) of the EXAFS (Figure 3b). After reaction in N_2O + C_2H_6, the absorption edge position shifted back to higher energy, and the magnitude of the FT increased. Isosbestic points in the Fe K-edge XANES spectra acquired during pretreatment (Figures S9 and S10) demonstrate the changes were stoichiometrically simple.

Shifts in energy of the absorption edge can be understood by comparison with spectra of iron oxide compounds (Figures S11–S13, Table S2) which show that Fe(II) compounds have lower edge energies than Fe(III) compounds. We therefore infer that the decrease in edge energy that resulted when the

DOI: 10.1021/jacs.9b08686
J. Am. Chem. Soc. 2019, 141, 18142–18151

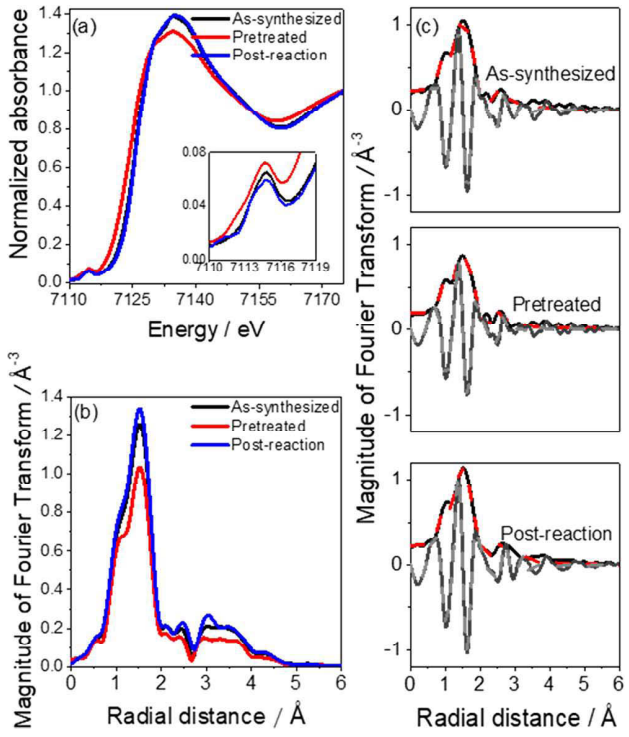

Figure 3. (a) Fe K-edge XANES, with inset showing an enlargement of the pre-edge peaks; (b) EXAFS data (magnitude of the Fourier transform (k^2-weighted)); and (c) EXAFS data and results of EXAFS modeling characterizing MIL-100(Fe) under various conditions: as-synthesized MIL-100(Fe) in flowing helium at 308 K, MIL-100(Fe) pretreated in flowing helium at 523 K, and MIL-100(Fe) postreaction, after exposure to N_2O + C_2H_6 flowing at 393 K. Imaginary part (solid gray line), and magnitude of the Fourier transform (k^2-weighted) of data (solid black line), and calculated contribution (dashed red line). All EXAFS data were collected after cooling the catalyst to 308 K.

as-synthesized MIL-100(Fe) was pretreated led to conversion of a fraction of the Fe(III) sites to Fe(II). After reaction with N_2O + C_2H_6, at 393 K the increase in edge energy (Figure 3a) suggests reoxidation of some Fe(II) back to Fe(III).

The EXAFS results (Figures S14–S40, Tables S3 and S4) characterizing the as-synthesized catalyst are consistent with the known structure of MIL-100(Fe) (Figure 3c and Table 1). After pretreatment in flowing helium at 523 K, EXAFS data (Table 1, Figure 3c) show that reduction of the iron based on the decrease in edge energy in XANES was accompanied by a decrease in average Fe–O coordination number from 6 to 5, indicated by the decrease in magnitude of the FT shown in Figure 3b. We attribute this decrease to the loss of physisorbed water and elimination of hydroxyl groups during treatment to form coordinatively unsaturated Fe(II) and Fe(III) sites[24−26] as evidenced by the disappearance of IR bands in the hydroxyl region (3700–3300 cm^{-1}) during identical treatment (Figure S1) and by differential PDF data showing a decrease in intensity of the deconvoluted Fe–O contributions after treatment in vacuo (Table S1). After this treatment, as the sample was exposed to catalytic reaction conditions in N_2O + C_2H_6, the average Fe–O CN recovered to that characterizing the as-synthesized material, a result bolstered by PDF data showing a recovery of Fe–O intensity. These results imply that, as a result of the catalysis, some Fe(III) sites on the nodes became occupied by molecules that we hypothesize were oxygenated products of the reaction that remain adsorbed within MIL-100(Fe) and require postreaction solvent washes with D_2O to desorb.

Information about the coordination geometry of the iron in the MOF nodes can be gained from the pre-edge features in the X-ray absorption spectra. With Fe in octahedral geometry in the as-synthesized MOF, the pre-edge peaks, which arise from 1s → 3d transitions, are split into two peaks for Fe(III) high-spin, the e_g and t_{2g} orbitals,[43] shown in Figure S12 in the SI. After pretreatment at 523 K, a third peak became evident (Figure S12b) at a lower energy than peaks characterizing octahedral Fe(III). This new peak is indicative of the single dipolar transition expected for high-spin Fe(II) in square pyramidal geometry[43] and serves as additional evidence for the reduction of a fraction of iron cations and the loss of an oxygen-containing ligand.

These changes in the pre-edge features, combined with observed shifts in the edge energy and reduction in Fe–O coordination demonstrated by the EXAFS data, provide evidence that during treatment in helium at 523 K, coordinatively unsaturated Fe(II) and Fe(III) sites form within MIL-100(Fe), and that after subsequent reaction in N_2O + C_2H_6 at 393 K Fe(II) sites are reoxidized and all iron sites become reoccupied to form octahedral species.

Further evidence for the formation of Fe(II) sites was sought using ex situ Mössbauer spectroscopy. Deconvolution of the spectra characterizing the as-synthesized sample showed three Lorentzian doublets (Figure 4a), with isomer shift and

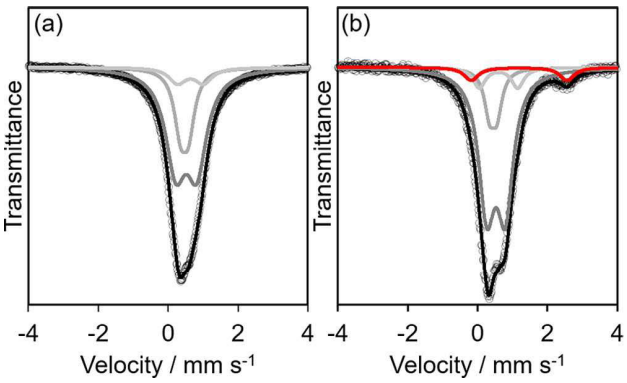

Figure 4. Mössbauer spectra of MIL-100(Fe) (a) as-synthesized, (b) after treatment at 523 K in vacuo. Color code: gray circles (raw data), black (fit to data), gray (Fe(III) doublets), red (Fe(II) doublet).

quadrupole splitting values listed in Table S5 in the SI. These values are consistent with high-spin (S = 5/2) Fe(III)[44] and compare well with literature values for MIL-100(Fe) formulated with alternative synthesis procedures.[23] Heating the sample to 523 K in vacuo before transfer to the spectrometer without air exposure resulted in changes in the isomer shift and quadrupole splitting of these three doublets (Table S6) that we assign to changes in ligand environment caused by a loss of weakly adsorbed solvent molecules, consistent with the IR spectra (Figure S2) and changes in iron coordination geometry shown by PDF and XAS data (vide supra). Importantly, an additional doublet, characteristic of high-spin (S = 2) Fe(II) species, appeared (Figure 4b) in the Mössbauer spectra, with values of isomer shift (0.98 mm s^{-1}) and quadrupole splitting (1.87 mm s^{-1}).[44] Previous multireference cluster calculations using a model of the Fe trimer node

DOI: 10.1021/jacs.9b08686
J. Am. Chem. Soc. 2019, 141, 18142–18151

similarly predict high spin states for both Fe(II) and Fe(III) sites (vide infra),[36] confirming the formation of active sites within the nodes of MIL-100(Fe) that mimic the oxidation state (+2) and spin state ($S = 2$) of active centers in a number of iron-containing enzymes capable of activating C−H bonds.

To provide evidence of the catalytic relevance of this high-spin ($S = 2$) Fe(II) site, we performed in situ chemical titrations using NO as a selective titrant for unsaturated Fe(II) species. NO was chosen as the titrant molecule because IR spectra show that mononitrosyl adducts form on Fe(II) sites at our reaction temperatures (398 K) when NO is dosed on MIL-100(Fe) under vacuum (Figure S41). In situ chemical titrations were performed by conducting independent batch reactor experiments with systematically varied amounts of NO in the initial $N_2O + C_3H_8$ reactant mixtures and observing how the initial rate of N_2 and C_3H_6 production change. Increasing amounts of NO added to the reactant mixture caused linear decreases in initial N_2 and C_3H_6 formation rates (Figure 5),

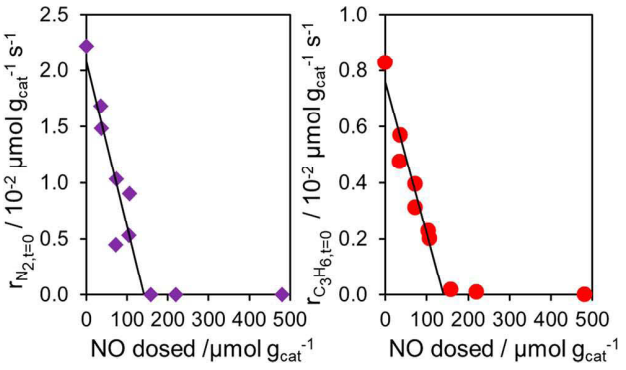

Figure 5. In situ chemical titration experiments showing the effect of increasing amounts of NO dosed into $N_2O + C_3H_8$ reactant mixtures on initial rates of N_2 and C_3H_6 product formation. (40−50 mg MIL-100(Fe), 393 K, $P_{total,t=0}$ = 114 kPa, $P_{N_2O,t=0}$ = 20 kPa, $P_{C_3H_8,t=0}$ = 2.5 kPa, $N_{NO,t=0}$ = 0−24 µmol).

until the formation of each product was fully suppressed at 142 ± 28 µmol g_{cat}^{-1} of NO dosed—this result represents complete titration of the active sites under reaction conditions. NO suppressed the N_2 and C_3H_6 formation reactions equally, and this result narrows the list of candidate rate-determining steps, with the data being consistent with the inference that the reaction of N_2O with Fe(II) sites is rate-determining. Linearity of the decrease in rates demonstrates a fixed ratio of NO titrant molecules to the Fe(II) site—evidence that all these sites are equivalent to each other. Further still, this fixed ratio is determined to be 1:1 based on equivalent ex situ NO dosing experiments (Figure S41) performed with IR spectroscopy, mentioned above, that reveal NO absorbed to form bands at 1820 and 1807 cm^{-1}, characteristic of mononitrosyl adducts on Fe(II) sites.[45] This stoichiometry determines a quantitative active Fe(II) site density: 142 ± 28 µmol g_{cat}^{-1}.

This value compares with a total iron content in the MOF of approximately 3500 µmol g_{cat}^{-1} (assuming 20 wt % iron on the basis of the crystallographic structure), giving a total fraction of Fe(III) reduced to be 4−5%. This result is consistent with the fraction of Fe(II) species calculated from Mössbauer spectra (6−7%). We stress that these values are less than the 33% corresponding to the overall MOF structure. We therefore conclude that MIL-100(Fe) consists of an array of nodes in which only a fraction contain active Fe(II) sites. The reason why some of the nodes lack active iron sites remains to be determined.

Reaction Kinetics and Mechanism. We sought insights into the mechanism of C_3H_8 activation with N_2O by investigating the reaction kinetics. The site density of Fe(II) counted using NO titrations was used to normalize initial rates of reaction. Reaction orders were determined by measuring reaction rates at various partial pressures of N_2O and C_3H_8 in the feed mixtures (Figure 6a−d). The data show reaction orders of 1 and 0 in N_2O and C_3H_8 partial pressures, respectively, for both N_2 and C_3H_6 formation, consistent with the aforementioned suggestions that the rate-determining step be the reaction of N_2O with Fe(II) and not C−H bond scission. Reaction experiments at various temperatures (Figure 6e,f) were performed to extract an apparent activation enthalpy of 79 ± 6 kJ mol^{-1}, corresponding to the intrinsic activation enthalpy minus the heat of adsorption of N_2O on the Fe(II) site in the MOF (Figure S44). Thus, we represent the reaction kinetics as follows:

$$\frac{r_i}{[\mathrm{Fe(II)}]} = k_{i,\mathrm{eff}} P_{N_2O} \quad i = N_2,\ C_3H_6$$

The ability of an Fe(II) site in the node of MIL-100(Fe) to activate C_3H_8 with N_2O as an oxidant was assessed with DFT to provide a basis for proposing a complete catalytic cycle for products directly formed from propane (constituting >80% of the total yield: 2-propanol, propylene, and 1-propanol) as shown in Scheme 1. A cluster model of a single Fe-trimer node of MIL-100(Fe), **A**, (Figure 7)[36] was used for these calculations. Spin-ladder computations of **A** predict that the iron high-spin state is preferred, in agreement with the Mössbauer spectra (Figure 4). Evidence for antiferromagnetic coupling between Fe(III) atoms within the nodes of MIL-100(Fe) has been provided by EPR spectroscopy.[46] When antiferromagnetic coupling of the Fe(III) centers is considered in the "broken symmetry" solution (BS, $2S + 1 = 5$), a further stabilization of 22 kJ mol^{-1} over the fully coupled high-spin state (HS, $2S + 1 = 15$) is predicted. More accurate energies for multireference systems are obtained using the BS solution, although the wave function is not a spin eigenfunction nor does it have the correct spin density.[47] Because of difficulties in following a reaction profile on a broken symmetry surface,[36,47] we report the mechanisms obtained for HS (Figure 7).

The first step is the formation of Fe(IV)=O (**B**) in the reaction of N_2O with Fe(II) (**A**) following physisorption of N_2O on the node (**AO**, 30 kJ mol^{-1}) through the transition state **TS1** (140 kJ mol^{-1}; Figure 7). This step leads to C−H abstraction from C_3H_8 through transition state **TS2** to form a propyl radical and a reduced Fe(III)−OH species (**D**). The hydrogen atom abstracted is from the secondary carbon for 2-propanol and propylene formation (mechanisms (a) and (b) in Scheme 1), or the primary carbon for the 1-propanol cycle (mechanism (c) in Scheme 1). For alcohol formation, the propyl radical directly rebounds to form a bound propanol species (**E**), which then desorbs to complete the catalytic cycle. The propyl radical can alternatively undergo a second hydrogen abstraction to form propylene and water. The rate-limiting reaction of N_2O with Fe(II) is consistent with the observed first-order dependence of the rate on N_2O partial pressure shown in Figures 6a,b with appropriate agreement between the experimental (79 ± 6 kJ mol^{-1}) and computed

DOI: 10.1021/jacs.9b08686
J. Am. Chem. Soc. 2019, 141, 18142−18151

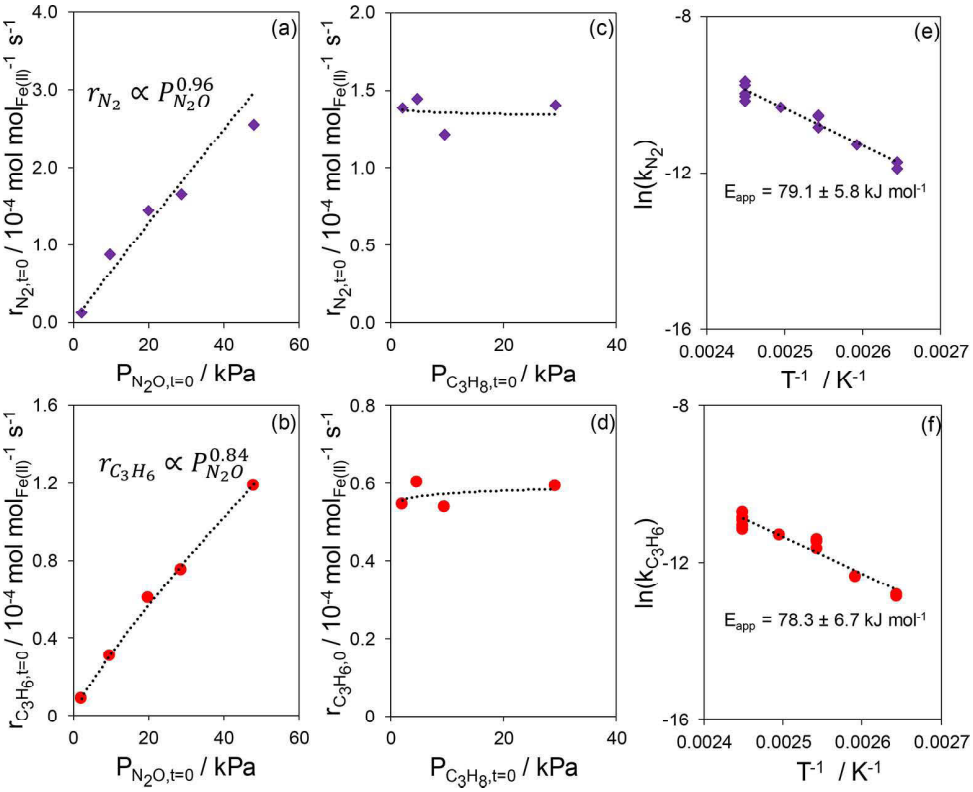

Figure 6. (a) Initial rate of N_2 formation versus initial N_2O pressure (393 K, $P_{C_3H_8,t=0}$ = 2.5 kPa) with accompanying power law fit. (b) Initial rate of C_3H_6 formation versus initial N_2O pressure with accompanying power law fit. (c) Initial rate of N_2 formation versus initial C_3H_8 pressure (393 K, $P_{N_2O,t=0}$ = 35 kPa). (d) Initial rate of C_3H_6 formation versus initial C_3H_8 pressure. Arrhenius plots of rate constants for N_2 (e) and C_3H_6 (f) at 378, 385.5, 393, 400.5, and 408 K with accompanying apparent activation enthalpies.

Scheme 1. Catalytic Cycles for Propane Conversion to 2-Propanol, Propylene, and 1-Propanol on Fe(II) Sites in MIL-100(Fe)

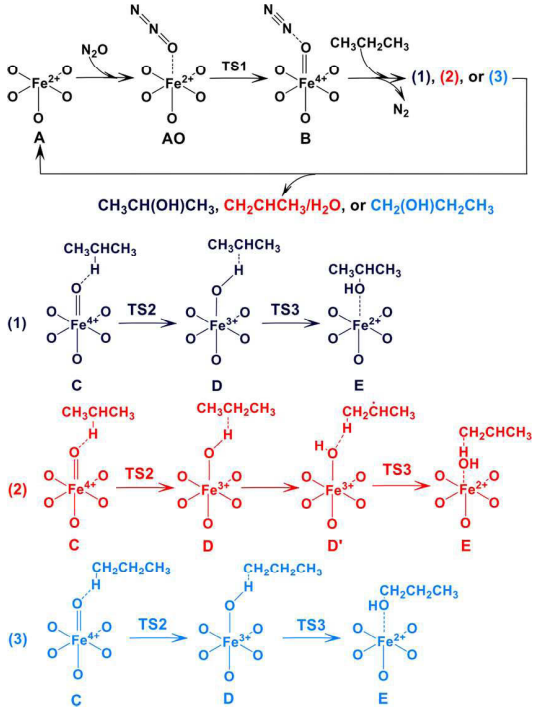

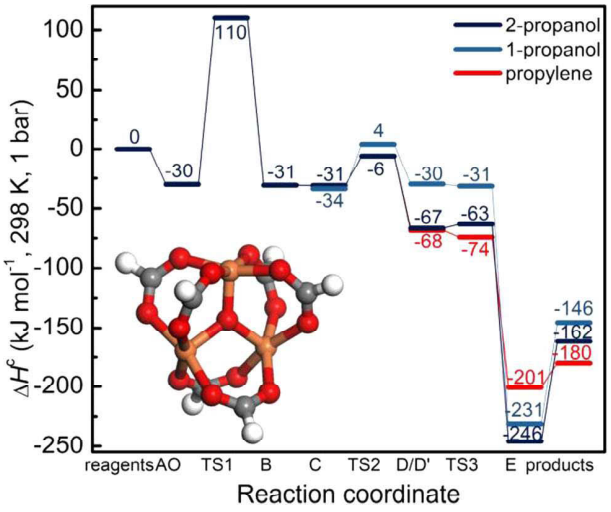

Figure 7. Enthalpy diagrams for the oxidation of propane by Fe(II) in MIL-100(Fe) to form 2-propanol (dark blue line), 1-propanol (light blue), and propylene (red) as computed at the UM06-L/def2-TZVP level of theory according to the cycles reported in Scheme 1. The enthalpies are reported taking separated reactants as zero. The optimized structure of the cluster in the reagent state (**A**) is reported using the color code: red (oxygen), orange (iron), gray (carbon), white (hydrogen).

activation enthalpies relative to separated reactants: 110 and 95 kJ mol^{-1}, for HS and BS spin states, respectively. This

DOI: 10.1021/jacs.9b08686
J. Am. Chem. Soc. 2019, 141, 18142−18151

agreement further improves upon inclusion of van der Waals interactions between N_2O and unrepresented MOF pore functionality in our minimal model (−10 kJ mol^{-1}, see Section S9.2). The combination of lower energy of the cluster **A** for the BS solution and the closest agreement between computational and experimental activation enthalpies, therefore, leads us to propose that antiferromagnetically coupled clusters are responsible for the activity of MIL-100(Fe).

The enthalpies determined computationally for the reaction profiles reported in Figure 7 also explain the relative yields obtained experimentally for 2-propanol > propylene ≫ 1-propanol. After Fe(IV)═O formation the HAA step **C** → **D**, from a primary carbon for 1-propanol formation and from a secondary carbon for 2-propanol (see Scheme 1), has the largest barrier. Propylene formation requires two HAA, from both a primary and a secondary carbon. The HAA from the secondary carbon of propane is favored both kinetically (25 kJ mol^{-1} vs 38 kJ mol^{-1}) and thermodynamically (−33 kJ mol^{-1} vs +4 kJ mol^{-1}) over that from the primary carbon, suggesting that the first HAA for propylene will be from the secondary carbon. This inference concurs with the lower yields of 1-propanol in comparrison to 2-propanol and propylene. The **D** → **E** step is almost barrierless for the three subsequent reactions with respect to energies; for enthalpies there is no barrier for 1-propanol and propylene formation, because the frequency dominated by hydrogenic motion is no longer part of the vibrational partition function. The product yields observed experimentally for 2-propanol and propylene are in line with the reaction enthalpy associated with the **D** → **E** step (179 and 133 kJ mol^{-1}, respectively). The last step of the reaction is release of the products with restoration of **A** to close the cycle. The desorption enthalpy of propylene is only 21 kJ mol^{-1}, decidedly lower than that predicted for the desorption of the alcohols (∼80 kJ mol^{-1}).

Comparisons with calculated barriers for reactions of N_2O with Fe(II) in numerous ligand environments and spin states[18] show that a high-spin state leads to a lower barrier than an intermediate or low spin state. Considering the Fe(II) site in the MIL-100(Fe) node to be in an intermediate spin (S = 1) state, the barrier associated with N_2O activation relative to separated reagents is computed to increase with respect to the high-spin (S = 2) case (146 for S = 1 vs 110 kJ mol^{-1} for S = 2, Figure S42), whereas the barrier associated with C−H bond scission is calculated to decrease (20 vs 25 kJ mol^{-1} for the secondary carbon, Figure S43). This observation suggests that ability of MIL-100(Fe) to stabilize high-spin (S = 2) Fe(II) sites, likely owing to a weak ligand field associated with surrounding O atoms in a square pyramidal environment, is vital for conferring reactivity to MIL-100(Fe) toward N_2O at the temperatures investigated (<408 K) and thus for activating light alkanes.

CONCLUSIONS

In presence of the atomic oxidant N_2O, MIL-100(Fe) activates light alkanes while retaining its bulk structural properties determined by N_2 adsorption, XRD, and IR and Raman spectra. XAS and Mössbauer spectra recorded in concert with chemical titrations provide evidence that activation of light alkanes occurs on high-spin (S = 2), square-pyramidal Fe(II) sites situated within the nodes of MIL-100(Fe). Kinetics experiments showed a first-order dependence of rate on N_2O partial pressure, consistent with DFT calculations performed with a cluster model of the catalyst that identify activation of Fe(II) sites by reaction with N_2O to be rate-determining, with good agreement between experimental and computational activation enthalpies. Improved agreement between the activation barriers, along with additional stabilization was found when considering antiferromagnetic coupling between the two adjacent Fe(III) atoms within each cluster, suggesting that these coupled clusters may be responsible for catalyst efficacy at these temperatures. This result suggests that electronic effects imparted from atoms beyond the first coordination shell of the active site may be able to induce improvements in catalyst performance, potentially opening new avenues for tailoring active site reactivity. We posit that fundamental understanding of the nature and function of supported catalysts, even those having structures as nearly uniform as MOFs, requires concerted characterization with quantitative catalyst performance measurements, catalyst site density determinations, spectra obtained with multiple techniques, and theory. Results such as those reported here open the possibility of using MIL-100(Fe) as a platform for design of improved catalysts for light alkane activation—guided by theory to take advantage of the modularity of MOFs and the opportunities they offer through choice of the structures and compositions of the organic linkers and inorganic nodes.

ASSOCIATED CONTENT

Supporting Information

The Supporting Information is available free of charge on the ACS Publications website at DOI: 10.1021/jacs.9b08686.

Detailed descriptions of synthesis, materials characterization, catalysis, and X-ray absorption spectroscopy experiments and DFT calculations (PDF)

AUTHOR INFORMATION

Corresponding Authors

*gagliard@umn.edu
*abhan@umn.edu

ORCID

Matthew C. Simons: 0000-0002-4279-043X
Jenny G. Vitillo: 0000-0002-6213-2039
Melike Babucci: 0000-0001-7785-3755
Christopher J. Cramer: 0000-0001-5048-1859
Karena W. Chapman: 0000-0002-8725-5633
Simon R. Bare: 0000-0002-4932-0342
Bruce C. Gates: 0000-0003-0274-4882
Connie C. Lu: 0000-0002-5162-9250
Laura Gagliardi: 0000-0001-5227-1396
Aditya Bhan: 0000-0002-6069-7626

Notes

The authors declare no competing financial interest.

ACKNOWLEDGMENTS

This work was supported by the Inorganometallic Catalyst Design Center, an Energy Frontier Research Center funded by the US Department of Energy (DOE), Office of Science, Basic Energy Sciences (BES) (DE-SC0012702). The authors acknowledge the Minnesota Supercomputing Institute (MSI) at the University of Minnesota for providing computational resources. Parts of this work were carried out in the Characterization Facility, University of Minnesota, which receives partial support from the National Science Foundation

DOI: 10.1021/jacs.9b08686
J. Am. Chem. Soc. 2019, 141, 18142−18151

(NSF) through the MRSEC program. Mössbauer spectroscopy was performed at the Institute for Rock Magnetism (IRM) at the University of Minnesota with the help of Peter Solheid. The IRM is a US National Multiuser Facility supported through the Instrumentation and Facilities program of the NSF, Earth Sciences Division, and by funding from the University of Minnesota. We acknowledge the Stanford Synchrotron Radiation Lightsource (SSRL) for access to beam time on Beamline 9-3. SSRL, SLAC National Accelerator Laboratory, is supported by DOE BES, under Contract No. DE-AC02-76SF00515, and the DOE BES-funded Consortium for Operando and Advanced Catalyst Characterization via Electronic Spectroscopy and Structure (Co-ACCESS) at SLAC National Accelerator Laboratory. Data for pair distribution function analysis were collected at beamline11-ID-B at Argonne National Laboratory, and use of the Advanced Photon Source, a User Facility operated for the US DOE, Office of Science, by Argonne National Laboratory, was supported by DOE Contract No. DE-AC02-06CH11357. We acknowledge Prof. R. Lee Penn, University of Minnesota, for helpful technical discussions.

REFERENCES

(1) Labinger, J. A. Selective alkane oxidation: hot and cold approaches to a hot problem. *J. Mol. Catal. A: Chem.* **2004**, *220*, 27−35.

(2) Tinberg, C. E.; Lippard, S. J. Dioxygen activation in soluble methane monooxygenase. *Acc. Chem. Res.* **2011**, *44*, 280−288.

(3) Ross, M. O.; Rosenzweig, A. C. A tale of two methane monooxygenases. *JBIC, J. Biol. Inorg. Chem.* **2017**, *22*, 307−319.

(4) Dinh, K. T.; Sullivan, M. M.; Serna, P.; Meyer, R. J.; Dincă, M.; Román-Leshkov, Y. Viewpoint on the Partial Oxidation of Methane to Methanol Using Cu- and Fe-Exchanged Zeolites. *ACS Catal.* **2018**, *8*, 8306−8313.

(5) Shu, L.; Nesheim, J. C.; Kauffmann, K.; Münck, E.; Lipscomb, J. D.; Que, L. An $Fe_2^{(IV)}O_2$ diamond core structure for the key intermediate Q of methane monooxygenase. *Science* **1997**, *275*, 515−518.

(6) Biswas, A. N.; Puri, M.; Meier, K. K.; Oloo, W. N.; Rohde, G. T.; Bominaar, E. L.; Münck, E.; Que, L. Modeling TauD- J: A high-spin nonheme oxoiron(IV) complex with high reactivity toward C-H bonds. *J. Am. Chem. Soc.* **2015**, *137*, 2428−2431.

(7) Dubkov, K. A.; Sobolev, V. I.; Panov, G. I. Low-temperature oxidation of methane to methanol on FeZSM-5 zeolite. *Kinet. Catal.* **1998**, *39*, 72−79.

(8) Starokon, E. V.; Parfenov, M. V.; Arzumanov, S. S.; Pirutko, L. V.; Stepanov, A. G.; Panov, G. I. Oxidation of methane to methanol on the surface of FeZSM-5 zeolite. *J. Catal.* **2013**, *300*, 47−54.

(9) Parfenov, M. V.; Starokon, E. V.; Pirutko, L. V.; Panov, G. I. Quasicatalytic and catalytic oxidation of methane to methanol by nitrous oxide over FeZSM-5 zeolite. *J. Catal.* **2014**, *318*, 14−21.

(10) Snyder, B. E. R.; Vanelderen, P.; Bols, M. L.; Hallaert, S. D.; Böttger, L. H.; Ungur, L.; Pierloot, K.; Schoonheydt, R. A.; Sels, B. F.; Solomon, E. I. The active site of low-temperature methane hydroxylation in iron-containing zeolites. *Nature* **2016**, *536*, 317−321.

(11) Snyder, B. E. R.; Böttger, L. H.; Bols, M. L.; Yan, J. J.; Rhoda, H. M.; Jacobs, A. B.; Hu, M. Y.; Zhao, J.; Alp, E. E.; Hedman, B.; Hodgson, K. O.; Schoonheydt, R. A.; Sels, B. F.; Solomon, E. I. Structural characterization of a non-heme iron active site in zeolites that hydroxylates methane. *Proc. Natl. Acad. Sci. U. S. A.* **2018**, *115*, 4565−4570.

(12) Bols, M. L.; Hallaert, S. D.; Snyder, B. E. R.; Devos, J.; Plessers, D.; Rhoda, H. M.; Dusselier, M.; Schoonheydt, R. A.; Pierloot, K.; Solomon, E. I.; Sels, B. F. Spectroscopic Identification of the α-Fe/α-O Active Site in Fe-CHA Zeolite for the Low-Temperature Activation of the Methane C-H Bond. *J. Am. Chem. Soc.* **2018**, *140*, 12021−12032.

(13) Wang, C.; An, B.; Lin, W. Metal-Organic Frameworks in Solid-Gas Phase Catalysis. *ACS Catal.* **2019**, *9*, 130−146.

(14) Hall, J. N.; Bollini, P. Structure, characterization, and catalytic properties of open-metal sites in metal organic frameworks. *Reaction Chemistry and Engineering* **2019**, *4*, 207−222.

(15) Rogge, S. M. J.; Bavykina, A.; Hajek, J.; Garcia, H.; Olivos-Suarez, A. I.; Sepúlveda-Escribano, A.; Vimont, A.; Clet, G.; Bazin, P.; Kapteijn, F.; Daturi, M.; Ramos-Fernandez, E. V.; Llabrés i Xamena, F. X.; Van Speybroeck, V.; Gascon, J.; Farha, O. K.; Serre, C.; Serre, C.; Devic, T.; Clet, G.; Pedersen, T. B.; Peng, D.; Plasser, F.; Pritchard, B.; Reiher, M.; Rivalta, I.; Schapiro, I.; Segarra-Martí, J.; Stenrup, M.; Truhlar, D. G.; Ungur, L.; Valentini, A.; Vancoillie, S.; Veryazov, V.; Vysotskiy, V. P.; Weingart, O.; Zapata, F.; Lindh, R. Metal−organic and covalent organic frameworks as single-site catalysts. *Chem. Soc. Rev.* **2017**, *46*, 3134−3184.

(16) Islamoglu, T.; Goswami, S.; Li, Z.; Howarth, A. J.; Farha, O. K.; Hupp, J. T. Postsynthetic Tuning of Metal-Organic Frameworks for Targeted Applications. *Acc. Chem. Res.* **2017**, *50*, 805−813.

(17) Xiao, D. J.; Bloch, E. D.; Mason, J. A.; Queen, W. L.; Hudson, M. R.; Planas, N.; Borycz, J.; Dzubak, A. L.; Verma, P.; Lee, K.; Bonino, F.; Crocella, V.; Yano, J.; Bordiga, S.; Truhlar, D. G.; Gagliardi, L.; Brown, C. M.; Long, J. R. Oxidation of ethane to ethanol by N_2O in a metal−organic framework with coordinatively unsaturated iron(II) sites. *Nat. Chem.* **2014**, *6*, 590−595.

(18) Verma, P.; Vogiatzis, K. D.; Planas, N.; Borycz, J.; Xiao, D. J.; Long, J. R.; Gagliardi, L.; Truhlar, D. G. Mechanism of Oxidation of Ethane to Ethanol at Iron(IV)−Oxo Sites in Magnesium-Diluted Fe_2(dobdc). *J. Am. Chem. Soc.* **2015**, *137*, 5770−5781.

(19) Osadchii, D. Y.; Olivos-Suarez, A. I.; Szecsenyi, A.; Li, G.; Nasalevich, M. A.; Dugulan, I. A.; Crespo, P. S.; Hensen, E. J. M.; Veber, S. L.; Fedin, M. V.; Sankar, G.; Pidko, E. A.; Gascon, J. Isolated Fe Sites in Metal Organic Frameworks Catalyze the Direct Conversion of Methane to Methanol. *ACS Catal.* **2018**, *8*, 5542−5548.

(20) Rosen, A. S.; Notestein, J. M.; Snurr, R. Q. Structure-Activity Relationships That Identify Metal-Organic Framework Catalysts for Methane Activation. *ACS Catal.* **2019**, *9*, 3576−3587.

(21) Rosen, A. S.; Notestein, J. M.; Snurr, R. Q. Identifying promising metal−organic frameworks for heterogeneous catalysis via high-throughput periodic density functional theory. *J. Comput. Chem.* **2019**, *40*, 1305−1318.

(22) Gani, T. Z. H.; Kulik, H. J. Understanding and Breaking Scaling Relations in Single-Site Catalysis: Methane to Methanol Conversion by Fe^{IV}=O. *ACS Catal.* **2018**, *8*, 975−986.

(23) Horcajada, P.; Surblé, S.; Serre, C.; Hong, D.-Y.; Seo, Y.-K.; Chang, J.-S.; Grenèche, J.-M.; Margiolaki, I.; Férey, G. Synthesis and catalytic properties of MIL-100(Fe), an iron(III) carboxylate with large pores. *Chem. Commun.* **2007**, 2820−2822.

(24) Yoon, J. W.; Seo, Y. K.; Hwang, Y. K.; Chang, J. S.; Leclerc, H.; Wuttke, S.; Bazin, P.; Vimont, A.; Daturi, M.; Bloch, E.; Llewellyn, P. L.; Serre, C.; Horcajada, P.; Grenèche, J. M.; Rodrigues, A. E.; Férey, G. Controlled reducibility of a metal-organic framework with coordinatively unsaturated sites for preferential gas sorption. *Angew. Chem., Int. Ed.* **2010**, *49*, 5949−5952.

(25) Leclerc, H.; Vimont, A.; Lavalley, J.-C.; Daturi, M.; Wiersum, A. D.; Llwellyn, P. L.; Horcajada, P.; Férey, G.; Serre, C. Infrared study of the influence of reducible iron(III) metal sites on the adsorption of CO, CO_2, propane, propene and propyne in the mesoporous metal−organic framework MIL-100. *Phys. Chem. Chem. Phys.* **2011**, *13*, 11748.

(26) Wuttke, S.; Bazin, P.; Vimont, A.; Serre, C.; Seo, Y. K.; Hwang, Y. K.; Chang, J. S.; Férey, G.; Daturi, M. Discovering the active sites for C3 separation in MIL-100(Fe) by using operando IR spectroscopy. *Chem. - Eur. J.* **2012**, *18*, 11959−11967.

(27) Yang, D.; Gates, B. C. Catalysis by Metal Organic Frameworks: Perspective and Suggestions for Future Research. *ACS Catal.* **2019**, *9*, 1779−1798.

(28) Feng, D.; Wang, K.; Wei, Z.; Chen, Y. P.; Simon, C. M.; Arvapally, R. K.; Martin, R. L.; Bosch, M.; Liu, T. F.; Fordham, S.;

DOI: 10.1021/jacs.9b08686
J. Am. Chem. Soc. 2019, 141, 18142−18151

Yuan, D.; Omary, M. A.; Haranczyk, M.; Smit, B.; Zhou, H. C. Kinetically tuned dimensional augmentation as a versatile synthetic route towards robust metal-organic frameworks. *Nat. Commun.* **2014**, *5*, 5723−5732.
(29) Guesh, K.; Caiuby, C. A. D.; Mayoral, Á.; Díaz-García, M.; Díaz, I.; Sanchez-Sanchez, M. Sustainable Preparation of MIL-100(Fe) and Its Photocatalytic Behavior in the Degradation of Methyl Orange in Water. *Cryst. Growth Des.* **2017**, *17*, 1806−1813.
(30) Yang, X.; Juhas, P.; Farrow, C. L.; Billinge, S. J. L. xPDFsuite: an end-to-end software solution for high throughput pair distribution function transformation, visualization and analysis*arXiv.* **2015**, http://arxiv.org/abs/1402.3163.
(31) Toby, B. H.; Von Dreele, R. B. GSAS-II: the genesis of a modern open-source all purpose crystallography software package. *J. Appl. Crystallogr.* **2013**, *46*, 544−549.
(32) Zhao, Y.; Truhlar, D. G. A new local density functional for main-group thermochemistry, transition metal bonding, thermochemical kinetics, and noncovalent interactions. *J. Chem. Phys.* **2006**, *125*, 194101−194118.
(33) Weigend, F.; Ahlrichs, R. Balanced basis sets of split valence, triple zeta valence and quadruple zeta valence quality for H to Rn: Design and assessment of accuracy. *Phys. Chem. Chem. Phys.* **2005**, *7*, 3297−3305.
(34) Weigend, F. Accurate Coulomb-fitting basis sets for H to Rn. *Phys. Chem. Chem. Phys.* **2006**, *8*, 1057−1065.
(35) Frisch, M. J.; Trucks, G. W.; Schlegel, H. B.; Scuseria, G. E.; Robb, M. A.; Cheeseman, J. R.; Scalmani, G.; Barone, V.; Mennucci, B.; Petersson, G. A.; Nakatsuji, H.; Caricato, M.; Li, X.; Hratchian, H. P.; Izmaylov, A. F.; Bloino, J.; Zheng, G.; Sonnen-berg, J. L.; Hada, M.; Ehara, M.; Toyota, K.; Fukuda, R.; Hasegawa, J.; Ishida, M.; Nakajima, T.; Honda, Y.; Kitao, O.; Nakai, H.; Vreven, T.; Montgomery, J. A., Jr.; Peralta, J. E.; Ogliaro, F.; Bearpark, M.; Heyd, J. J.; Brothers, E.; Kudin, K. N.; Staroverov, V. N.; Kobayashi, R.; Normand, J.; Raghavachari, K.; Rendell, A.; Burant, J. C.; Iyengar, S. S.; Tomasi, J.; Cossi, M.; Rega, N.; Millam, J. M.; Klene, M.; Knox, J. E.; Cross, J. B.; Bakken, V.; Adamo, C.; Jaramillo, J.; Gomperts, R.; Stratmann, R. E.; Yazyev, O.; Austin, A. J.; Cammi, R.; Pomelli, C.; Ochter-ski, J. W.; Martin, R. L.; Morokuma, K.; Zakrzewski, V. G.; Voth, G. A.; Salvador, P.; Dannenberg, J. J.; Dapprich, S.; Daniels, A. D.; Farkas, Ö.; Foresman, J. B.; Ortiz, J. V.; Cioslowski, J.; Fox, D. J. *Gaussian 09*; Gaussian, Inc.: Wallingford, CT, 2016.
(36) Vitillo, J. G.; Bhan, A.; Cramer, C. J.; Lu, C. C.; Gagliardi, L. Quantum Chemical Characterization of Structural Single Fe(II) Sites in MIL-Type Metal-Organic Frameworks for the Oxidation of Methane to Methanol and Ethane to Ethanol. *ACS Catal.* **2019**, *9*, 2870−2879.
(37) Lv, H.; Zhao, H.; Cao, T.; Qian, L.; Wang, Y.; Zhao, G. Efficient degradation of high concentration azo-dye wastewater by heterogeneous Fenton process with iron-based metal-organic framework. *J. Mol. Catal. A: Chem.* **2015**, *400*, 81−89.
(38) Starokon, E. V.; Parfenov, M. V.; Pirutko, L. V.; Abornev, S. I.; Panov, G. I. Room-temperature oxidation of methane by α-oxygen and extraction of products from the FeZSM-5 surface. *J. Phys. Chem. C* **2011**, *115*, 2155−2161.
(39) Li, Z.; Peters, A. W.; Bernales, V.; Ortuño, M. A.; Schweitzer, N. M.; DeStefano, M. R.; Gallington, L. C.; Platero-Prats, A. E.; Chapman, K. W.; Cramer, C. J.; Gagliardi, L.; Hupp, J. T.; Farha, O. K. Metal−Organic Framework Supported Cobalt Catalysts for the Oxidative Dehydrogenation of Propane at Low Temperature. *ACS Cent. Sci.* **2017**, *3*, 31−38.
(40) Li, Z.; Peters, A. W.; Platero-Prats, A. E.; Liu, J.; Kung, C. W.; Noh, H.; DeStefano, M. R.; Schweitzer, N. M.; Chapman, K. W.; Hupp, J. T.; Farha, O. K. Fine-Tuning the Activity of Metal-Organic Framework-Supported Cobalt Catalysts for the Oxidative Dehydrogenation of Propane. *J. Am. Chem. Soc.* **2017**, *139*, 15251−15258.
(41) Sava Gallis, D. F.; Chapman, K. W.; Rodriguez, M. A.; Greathouse, J. A.; Parkes, M. V.; Nenoff, T. M. Selective O_2 Sorption at Ambient Temperatures via Node Distortions in Sc-MIL-100. *Chem. Mater.* **2016**, *28*, 3327−3336.
(42) Forde, M. M.; Armstrong, R. D.; Hammond, C.; He, Q.; Jenkins, R. L.; Kondrat, S. A.; Dimitratos, N.; Lopez-Sanchez, J. A.; Taylor, S. H.; Willock, D.; Kiely, C. J.; Hutchings, G. J. Partial oxidation of ethane to oxygenates using Fe- and Cu-containing ZSM-5. *J. Am. Chem. Soc.* **2013**, *135*, 11087−11099.
(43) Westre, T. E.; Kennepohl, P.; DeWitt, J. G.; Hedman, B.; Hodgson, K. O.; Solomon, E. I. A Multiplet Analysis of Fe K-Edge 1s → 3d Pre-Edge Features of Iron Complexes. *J. Am. Chem. Soc.* **1997**, *119*, 6297−6314.
(44) Münck, E. Aspects of ^{57}Fe Mossbauer Spectroscopy. In *Phys. Methods Bioinorg. Chem.*; Que, L., Jr., Ed.; University Science Books, 2000; pp 287−319.
(45) Nechita, M. T.; Berlier, G.; Ricchiardi, G.; Bordiga, S.; Zecchina, A. New precursor for the post-synthesis preparation of Fe-ZSM-5 zeolites with low iron content. *Catal. Lett.* **2005**, *103*, 33−41.
(46) Mali, G.; Mazaj, M.; Arčon, I.; Hanžel, D.; Arčon, D.; Jagličić, Z. Unraveling the Arrangement of Al and Fe within the Framework Explains the Magnetism of Mixed-Metal MIL-100(Al,Fe). *J. Phys. Chem. Lett.* **2019**, *10*, 1464−1470.
(47) Gaggioli, C. A.; Stoneburner, S. J.; Cramer, C. J.; Gagliardi, L. Beyond Density Functional Theory: The Multiconfigurational Approach To Model Heterogeneous Catalysis. *ACS Catal.* **2019**, *9*, 8481−8502.

DOI: 10.1021/jacs.9b08686
J. Am. Chem. Soc. 2019, 141, 18142−18151